AGU PUBLICATIONS

JGR

Journal of Geophysical Research: Solid Earth

RESEARCH ARTICLE
10.1002/2016JB013164

Key Points:
- A multiparametric approach allowed constraining magma dynamics leading to an eruption at Etna
- We provide an improved picture of the multilevel structure of Mount Etna's plumbing system

Supporting Information:
- Supporting Information S1
- Table S1
- Table S2
- Table S3

Correspondence to:
M. Viccaro,
m.viccaro@unict.it

Citation:
Viccaro, M., F. Zuccarello, A. Cannata, M. Palano, and S. Gresta (2016), How a complex basaltic volcanic system works: Constraints from integrating seismic, geodetic, and petrological data at Mount Etna volcano during the July–August 2014 eruption, *J. Geophys. Res. Solid Earth*, *121*, 5659–5678, doi:10.1002/2016JB013164.

Received 11 MAY 2016
Accepted 18 JUL 2016
Accepted article online 20 JUL 2016
Published online 4 AUG 2016

How a complex basaltic volcanic system works: Constraints from integrating seismic, geodetic, and petrological data at Mount Etna volcano during the July–August 2014 eruption

Marco Viccaro[1,2], Francesco Zuccarello[1], Andrea Cannata[2,3], Mimmo Palano[2], and Stefano Gresta[1]

[1]Dipartimento di Scienze Biologiche, Geologiche e Ambientali, Sezione di Scienze della Terra, Università degli Studi di Catania, Catania, Italy, [2]Osservatorio Etneo, Istituto Nazionale di Geofisica e Vulcanologia, Catania, Italy, [3]Dipartimento di Fisica e Geologia, Università degli Studi di Perugia, Perugia, Italy

Abstract Integrating geodetic, seismic, and petrological data for a recent eruptive episode at Mount Etna has enabled us to define the history of magma storage and transfer within the multilevel structure of the volcano, providing spatial and temporal constraints for magma movements before the eruption. Geodetic data related to the July–August 2014 activity provide evidence of a magma reservoir at ~4 km below sea level. This reservoir pressurized from late March 2014 and fed magmas that were then erupted from vents on the lower eastern flank of North-East Crater (NEC) and at New South-East Crater (NSEC) summit crater during the July eruptive activity. Magma drainage caused its depressurization since mid-July. Textural and microanalytical data obtained from plagioclase crystals indicate similar disequilibrium textures and compositions at the cores in lavas erupted at the base of NEC and NSEC, suggesting comparable deep histories of evolution and ascent. Conversely, the compositional differences observed at the crystal rims have been associated to distinct degassing styles during storage in a shallow magma reservoir. Seismic data have constrained depth for a shallow part of the plumbing system at 1–2 km above sea level. Timescales of magma storage and transfer have also been calculated through diffusion modeling of zoning in olivine crystals of the two systems. Our data reveal a common deep history of magmas from the two systems, which is consistent with a recharging phase by more mafic magma between late March and early June 2014. Later, the magma continued its crystallization under distinct chemical and physical conditions at shallower levels.

1. Introduction

Constraints on subsurface fluid (i.e., magma, volatiles, or hydrothermal waters) movements, as well as the geometry, size, and depth range of magmatic reservoirs beneath active volcanoes, are usually provided by modeling geodetic data (see *Dzurisin* [2007] for an overview). Additional information can be acquired from seismic observations that in some basaltic volcanoes (e.g., Etna and Stromboli) are dominated by volcanic tremor, whose source mechanism is generally associated with fluid dynamics in the shallower portions of the volcano plumbing system [e.g., *Chouet*, 1996; *Chouet and Matoza*, 2013]. Other constraints, related to the timing of magma storage and transfer, can be defined by petrological data, considering mineral phases sensitive to changes in the thermodynamic equilibrium of the magmatic system, such as plagioclase and olivine [e.g., *Davidson et al.*, 2001, 2007; *Costa and Chakraborty*, 2004; *Morgan and Blake*, 2006; *Kahl et al.*, 2011; *Druitt et al.*, 2012]. Compositions and textures of plagioclase crystals vary depending on the melt composition along with temperature, pressure, H_2O contents, and fO_2 of the system, whereas olivine is mostly sensitive to changes in the melt composition and fO_2 [e.g., *Streck*, 2008, and references therein]. The use of textural and compositional data of minerals, in combination with intracrystalline diffusion modeling of specific elements, proved a sound method to decipher the spatial and temporal dynamics of magma evolution prior to eruption at several volcanoes [e.g., *Zellmer et al.*, 1999, 2003; *Davidson et al.*, 2001, 2007; *Costa et al.*, 2008; *Morgan et al.*, 2004; *Kahl et al.*, 2011, 2013, 2015; *Druitt et al.*, 2012; *Viccaro et al.*, 2016a].

Complex systems, such as Mount Etna volcano, require an integrated approach to produce realistic information on the geometry, depth of magmatic reservoirs, and preeruptive timescales of magma storage and transfer processes. Such kinds of multidisciplinary studies are becoming popular in modern volcanology, as they are solving important questions at active volcanoes worldwide (e.g., Turrialba [*Martini et al.*, 2010], El Hierro [*Martí et al.*, 2013], Manda Hararo rift [*Barnie et al.*, 2015], and Eyjafjallajökull [*Viccaro et al.*, 2016b]). Works

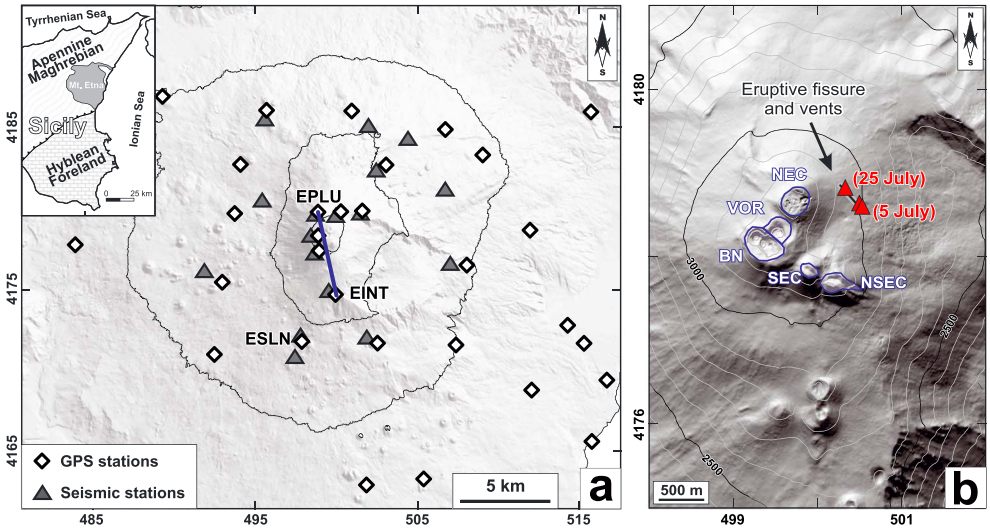

Figure 1. (a) Digital elevation model of Mount Etna with the location of the seismic and GPS stations, used in this study. The EPLU-EINT baseline is traced with a blue line. The seismic station ESLN is also indicated. Upper left inset shows a simplified structural map of eastern Sicily and the geographic location of Mount Etna. (b) Magnification of the volcano summit craters (Bocca Nuova, BN; Voragine, VOR; North-East Crater, NEC; South-East Crater, SEC; and New South-East Crater, NSEC) and eruptive fissure and vents opened during the analyzed eruptive period. Coordinates are UTM 33N projection.

integrating various types of data have already proved to be very useful at Mount Etna volcano in order to discern the dynamics of some recent eruptions [e.g., *Kahl et al*., 2013; *Viccaro et al*., 2014; *Cannata et al*., 2015; *Spampinato et al*., 2015].

On 5 July 2014, an eruptive fissure opened on the lower eastern flank of the North-East Crater (NEC). This activity was followed by eruptions at the New South-East Crater (NSEC) throughout the first half of August. The geophysical and petrological data presented in this study provide the spatial localization of deep and shallow magmatic sources and their temporal activation prior to and during the eruption. The wider implications of this paper are that realistic reconstructions of the spatial-temporal history of magmas prior to an eruption can only be accomplished by integrating the physical and chemical constraints from multiple disciplines.

2. Volcanological Background

Mount Etna is an open-vent Quaternary basaltic volcano, located at the front of the Apennine-Maghrebian thrust belt on the east coast of Sicily (Figure 1a). There are currently five summit craters (Figure 1b): South-East Crater (SEC), New South-East Crater (NSEC), Bocca Nuova (BN), Voragine (VOR), and North-East Crater (NEC). Eruptions at Mount Etna range from frequent activity at the summit craters and episodic flank eruptions. The former is characterized by phases of degassing alternating with mild Strombolian activity, occasional lava fountains, and lava overflows. Flank eruptions occur from lateral vents usually located along fracture systems [e.g., *Acocella and Neri*, 2003; *Andronico et al*., 2005; *Burton et al*., 2005; *Spampinato et al*., 2008].

After the end of the May 2008 to July 2009 eruption, Mount Etna was characterized only by degassing and some sporadic minor explosive phenomena for 17 months [*Andronico et al*., 2013]. In January 2011, an eruptive phase started and lasted up to April 2012, involving 25 episodes of lava fountaining at NSEC, as well as Strombolian activity and intracrater lava flows at BN [e.g., *Behncke et al*., 2014]. The lava fountain episodes finally led to the creation of the huge NSEC cone.

During 2013, two periods of major eruptive activity were observed [e.g., *Cannata et al*., 2015; *De Beni et al*., 2015; *Spampinato et al*., 2015]. From January to April, a series of short episodes of intense Strombolian activity took place at BN and VOR, as well as 13 lava fountain eruptions at NSEC. After a fairly quiescent period between May and August, six lava fountains and Strombolian activities occurred at NSEC throughout September to the beginning of December.

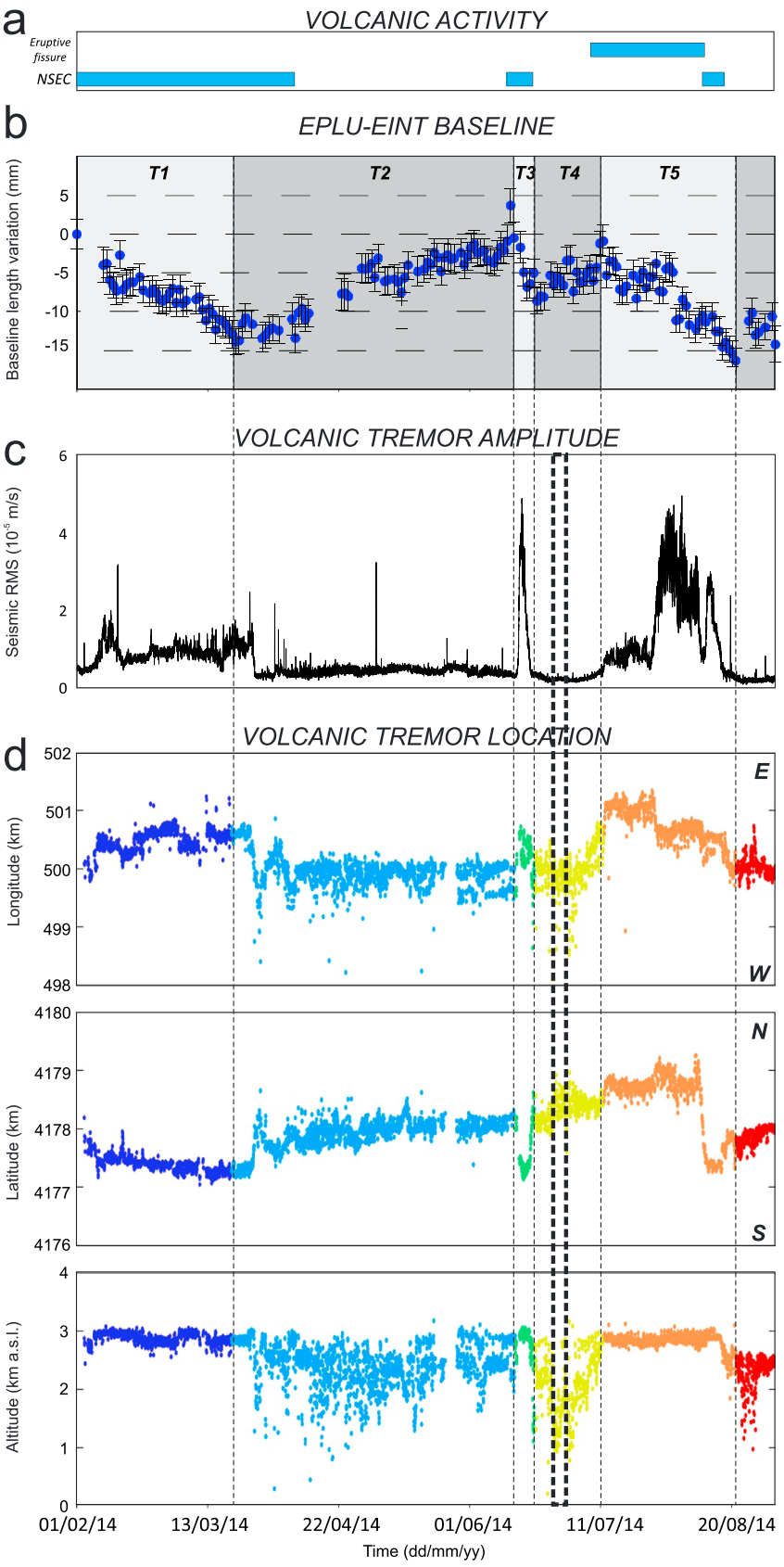
a
VOLCANIC ACTIVITY
Eruptive fissure
NSEC
b
EPLU-EINT BASELINE
T1
T2
T3
T4
T5
Baseline length variation (mm)
5
0
-5
-10
-15
c
VOLCANIC TREMOR AMPLITUDE
Seismic RMS (10^{-5} m/s)
6
4
2
0
d
VOLCANIC TREMOR LOCATION
Longitude (km)
502
501
500
499
498
E
W
Latitude (km)
4180
4179
4178
4177
4176
N
S
Altitude (km a.s.l.)
4
3
2
1
0
01/02/14
13/03/14
22/04/14
01/06/14
11/07/14
20/08/14
Time (dd/mm/yy)

Figure 2

All the NSEC lava fountain episodes, that took place from 2011 to 2013, lasted from a few days to a few hours and showed similar cycles of eruptive phases [e.g., *Behncke et al*., 2014; *Viccaro et al*., 2014; *Greco et al*., 2016]: (i) beginning with minor explosive activity, (ii) more vigorous Strombolian activity often accompanied by lava discharge, (iii) lava fountaining with voluminous tephra ejection and emplacement of lava flows, and (iv) rapid decline of lava fountaining and transition to mildly Strombolian activity.

However, since the second half of December 2013, the NSEC eruptive behavior changed: the initial Strombolian activity of the explosive episodes (the aforementioned eruptive phase "ii") did not culminate in sustained lava fountaining and voluminous tephra emission (the aforementioned eruptive phase "iii" was missing); in addition, the duration of the explosive episodes was longer (in the order of some days [*De Beni et al*., 2015]). This behavior became even more pronounced in 2014, when the activity of 21 January at NSEC was limited to Strombolian explosions at the summit of the crater and lava effusion from vents on its lower eastern flank. This activity lasted for 75 days and fluctuated in intensity, ending in the night of 6–7 April (Figure 2a) [*De Beni et al*., 2015]. The following eruptive episode took place at NSEC in mid-June 2014 and was preceded by about 5 weeks of intermittent Strombolian activity. Also, the mid-June episode was characterized by Strombolian activity and lava emission, but neither lava fountains nor voluminous tephra fall occurred [*De Beni et al*., 2015].

On 5 July 2014, an eruptive fissure opened on the lower eastern flank of NEC, feeding weak Strombolian activity and slow lava effusion from two new vents located at about 3000 m above sea level (asl) (Figure 1b; for time reference see Figure 2a). On 25 July, more intense Strombolian activity took place at a newly opened vent at 3090 m asl along the same fracture system (Figure 1b), close to the 5 July vent. The eruptive activity from these vents ended on early 10 August [*De Beni et al*., 2015]. Before the end of the activity on this fracture system, on 8 August, eruptive activity resumed also at NSEC, which culminated on 11–14 August with vigorous Strombolian explosions and lava effusion (Figure 2a). Eruptive phenomena at NSEC ended on 16 August. The second half of August was only characterized by degassing.

3. Geophysical Data

The eruptive episode analyzed in this study lasted from the beginning of July up to mid-August 2014. However, all the available geophysical data spanning the February–August interval have been analyzed in order to contextualize the eruptive episode within the framework of a longer time interval. This provides a comprehensive picture of events leading up to this episode.

3.1. Geodetic Data

Raw data collected from the permanent GPS network (Figure 1a) and spanning the 1 February 2014 to 31 August 2014 interval were analyzed using the GAMIT/GLOBK software [*Herring et al*., 2010] and adopting the methodology described in *González and Palano* [2014]. Precise ephemerides and absolute antenna phase center models provided by the International GNSS Service (www.igs.org) were used. In addition, the *Saastamoinen* [1972] atmospheric zenith delay models, coupled with the Global Mapping Functions [*Böhm et al*., 2006] for the neutral atmosphere, have been adopted. The results of this first step are daily estimates of loosely constrained station coordinates, and other parameters, along with the associated variance-covariance matrices. Lastly, the loosely constrained daily solutions were used as input in a Kalman filter (GLOBK) in order to estimate a consistent set of daily coordinates (i.e., time series) for all sites involved.

We focus on the daily baseline changes for EPLU and EINT stations because they were quasi-continuously operating throughout the investigated period (Figures 1a and 2b). Since these stations are located northwest (EPLU) and south (EINT) of the summit area, their relative motion over time is sensitive to any change in summit

Figure 2. Plot summarizing vent activity, seismic, and deformation data from February to August 2014. (a) Intervals of the main activity at NSEC and at the eruptive fissure opened on the lower eastern flank of NEC (here indicated as "eruptive fissure"). (b) Variation in length of the EPLU-EINT baseline with associated 1 sigma uncertainties. T1, T2, T3, T4, and T5 are time intervals discussed in the text. (c) RMS of the seismic signal recorded by the vertical component of ESLN station and filtered in the band 0.5–5.5 Hz. (d) Variation in time of the location of the volcanic tremor centroids (the color of the dots are different in each time interval, identified by GPS). The dashed rectangle in Figures 2c and 2d indicates the time interval shown in Figure 4b. The vertical dashed lines divide the investigated period into the time intervals, identified by GPS. The "E," "W," "N," and "S" labels in Figure 2d indicate the East-West and North-South directions.

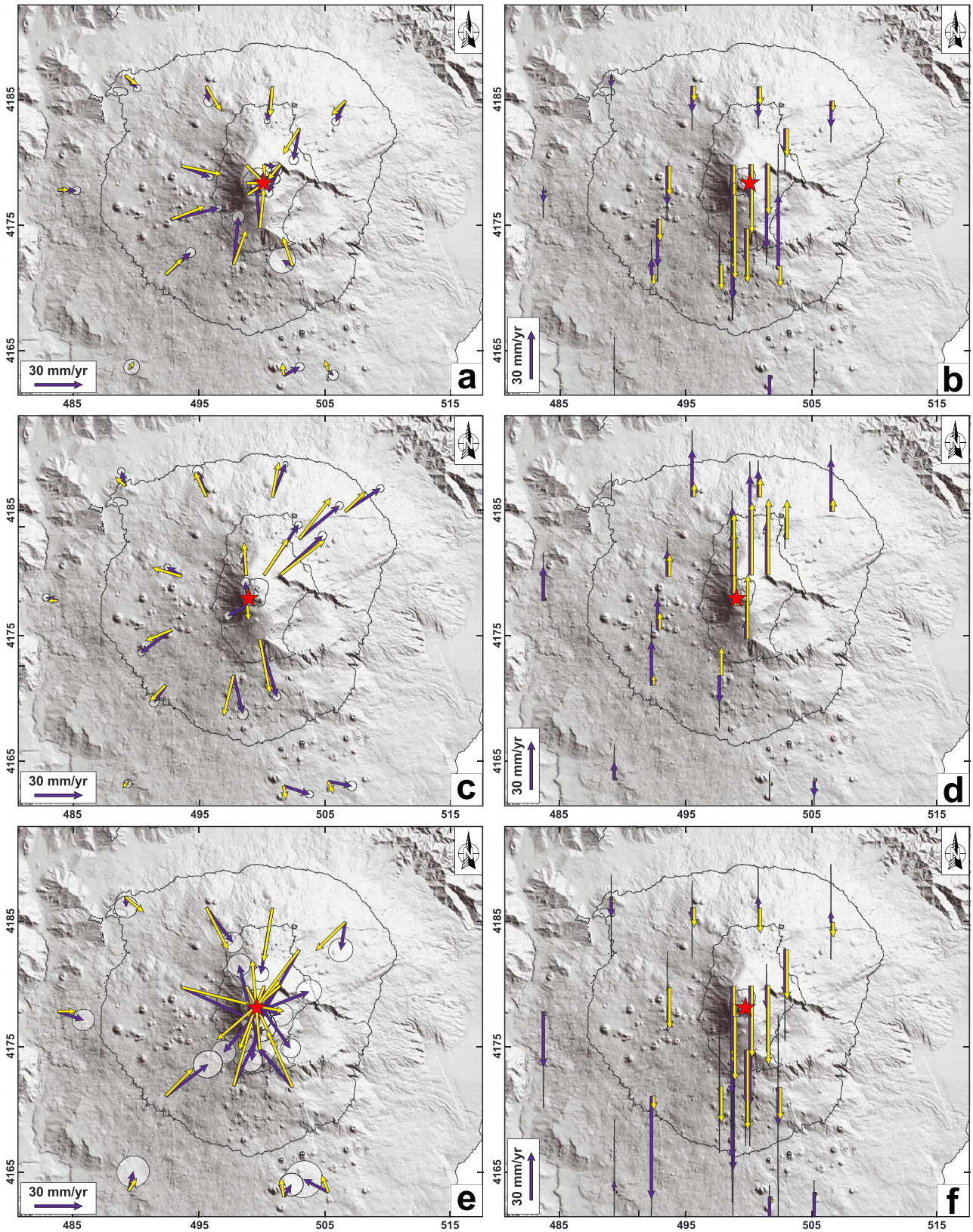

Figure 3. Comparison between observed (blue arrows) and modeled (yellow arrows) horizontal and vertical geodetic velocities related to (a and b) T1 (1 February 2014 to 20 March 2014), (c and d) T2 (20 March 2014 to 13 June 2014), and (e and f) T5 (11 July to 20 August). The red stars indicate the surface projection of modeled sources (see Table 1 for details). Uncertainties associated to GPS velocities are at the 95% level of confidence (ellipsoids for horizontal and bars for vertical components).

deformation. At least five major ground deformation stages are apparent in the data (Figure 2b): (T1) from 1 February to 20 March, the baseline shortened by ~1.5 cm; (T2) from 20 March up to 14 June, the baseline lengthened by ~1.4 cm; (T3) from 14 June to 20 June, the baseline shortened by ~0.7 cm; (T4) from 20 June to 11 July, the baseline lengthened by ~0.6 cm; (T5) from 11 July to 20 August, the baseline shortened by ~1.7 cm. Since 20 August, the baseline lengthened again, marking the beginning of a new pressurization of the magmatic plumbing system, which led to the emplacement of a shallow dike on 28 December. This last time interval has been analyzed by *Gambino et al*. [2016]; interested readers can refer to this study for additional details.

Although these stages have been delineated only on the basis of deformation pattern, in the following we refer to them, because of the temporal correlation between deformation, volcanic activity, and tremor amplitude and location.

For each detected stage, we estimated the ground deformation field in terms of geodetic velocities by combining the daily GAMIT solutions into a consistent set of station positions and velocities and adopting a local reference frame—Etn@ref—to isolate the volcanic deformation from the background tectonic pattern (see *Palano et al*. [2010] for details). Significant ground deformation occurred only during T1, T2, and T5 time intervals, while during T3 and T4, with the exclusion of a limited number of stations close to the summit area, the overall ground deformation signals have comparable magnitudes to their associated uncertainties (up to ~7 and 15 mm/yr at 1σ confidence interval for horizontal and vertical components, respectively). Such a low signal/noise ratio does not allow to properly investigate T3 and T4 patterns through inversion models. Conversely, T1 and T5 are characterized by a general contraction of the upper part of the volcano edifice, indicating a depressurization of the volcano plumbing system (Figures 3a, 3b, 3e, and 3f). T2 shows a general outward radial pattern, indicating a pressurization of the plumbing system (Figures 3c and 3d).

The surface deformation for T1, T2, and T5 was used to constrain isotropic half-space elastic inversion models. The inversions were performed using the genetic algorithm approach [e.g., *Tiampo et al*., 2000] and, to include topography, we also adopted the method of *Williams and Wadge* [2000]. To model the observed ground deformation pattern, we used the *Yang et al*.'s [1988] analytical model. Values of 30 GPa and 0.25 were assumed for the shear modulus and Poisson's ratio in the half-space, respectively; the chosen rigidity represents an average value for Etna's crust [*Chiarabba et al*., 2000] and corresponds to a typical value commonly used in modeling works for Mount Etna [e.g., *Bonanno et al*., 2011]. Estimation of the uncertainties in best fitting parameters was performed by adopting a Jackknife sampling method [*Efron*, 1982]. In the computation, both horizontal and vertical GPS components were inverted by taking into account the weights proportional to the associated displacement errors. We discarded all stations located on the middle-to-lower eastern flank of the volcano because they are affected by long-term seaward motion [*Palano et al*., 1998]; their overall ground displacement for the period 1 February to 31 August 2014, in agreement with the long-term seaward motion, is reported in Figure S1 in the supporting information.

For T1 (Figures 3a and 3b), the modeled source is located beneath the summit area at a depth of ~5.6 km below sea level (bsl). It has a prolate spheroid shape, slightly dipping toward NE, and is characterized by a negative volume change of $1.80 \cdot 10^6$ m^3 (Table 1). For T2 (Figures 3c and 3d), the best model is given by a near vertical elongated spheroid source centered at ~4.2 km (bsl) beneath the upper western flank of the volcano and is characterized by a positive volume change of $1.87 \cdot 10^6$ m^3 (Table 1). For T5 (Figures 3e and 3f), the best model is given by a prolate spheroid centered at ~3.7 km (bsl) beneath the summit area and characterized by a negative volume change of $1.24 \cdot 10^6$ m^3 (Table 1).

Overall, the final results show a reasonable fit between modeled and observed displacements (Figure 3c). Locally, some mismatches in both 3-D direction and magnitude between the modeled and observed geodetic velocities can be seen. These are possibly linked to local effects, such as monument instability and/or motion along nearby active faults.

3.2. Seismological Data

Seventeen seismic stations are located around Mount Etna's summit area up to 10 km away from its center (Figure 1a). All consist of broadband three-component Trillium seismometers (Nanometrics), with cutoff period of 40 s and sampling rates at 100 Hz. The recordings of these stations are routinely used to monitor and investigate the seismovolcanic signals generated at Mount Etna, and in particular volcanic tremor, long period events, and very long period events [e.g., *Cannata et al*., 2013].

Table 1. Estimated Parameters and Associated Uncertainties (at 95% of Confidence) for Sources Modeled for Intervals T1, T2, and T5[a]

Parameters	T1	T2	T5
Easting (m)	500432 ± 371	499379 ± 248	499393 ± 141
Northing (m)	4178419 ± 330	4177980 ± 202	4178182 ± 223
Depth (m bsl)	5639 ± 483	4166 ± 418	3747 ± 352
a axis (m)	591 ± 158	464 ± 152	482 ± 123
a/*b* ratio	0.38 ± 0.17	0.59 ± 0.16	0.48 ± 0.13
Azimuth (deg)	76.7 ± 16.4	80.5 ± 12.4	68.6 ± 7.0
Dip (deg)	37.6 ± 15.7	123.8 ± 13.5	31.9 ± 7.2
Ex. Pressure (Pa)	$-5.80 \pm 1.83 \times 10^8$	$5.17 \pm 1.12 \times 10^8$	$-4.65 \pm 1.55 \times 10^8$
ΔV (10^6 m^3)	−1.80	1.87	−1.24

[a] *a* and *b* are the lengths of the major and the minor axes, respectively. ΔV is calculated as $\Delta V = (\Delta P a b \wedge 2\pi)/\mu$ according to *Tiampo et al.* [2000], where μ is the rigidity modulus of the elastic half-space. ΔV is expressed as total volume changes. Coordinates are in UTM 33N projection.

Volcanic tremor was the dominant seismic signal during February–August 2014, and we investigated both amplitude and source locations to understand temporal and spatial changes. In order to track the variation through time of the amplitude, we calculated the root-mean-square (RMS) of the seismic signal recorded by the vertical component of ESLN seismic station (Figure 1a) within 10 min long sliding windows and filtered in the band 0.5–5.5 Hz (Figure 2c). This frequency band was chosen to include most of the volcanic tremor energy [e.g., *Cannata et al.*, 2008]. Locations of the volcanic tremor were obtained within 1 h long sliding time windows in order to track the spatial evolution of its source (Figures 2d and 4). We used a grid-search method based on spatial-seismic-amplitude distribution, assuming propagation in a homogeneous medium [*Di Grazia et al.*, 2006], applied on the three-component seismic signals filtered in the frequency band 0.5–2.5 Hz, to determine tremor locations. The location error was calculated by the jackknife method [*Di Grazia et al.*, 2006; *Cannata et al.*, 2013] and was equal to ~0.3, ~0.4, and ~0.7 km for longitude, latitude, and altitude, respectively. It is worth noting that if more than one tremor source are active: (i) the tremor location will indicate the position of the dominant source, in case of sources with distinct intensity; or (ii) the tremor location will be placed in a position in between the real locations of the volcanic tremor sources, in case of sources

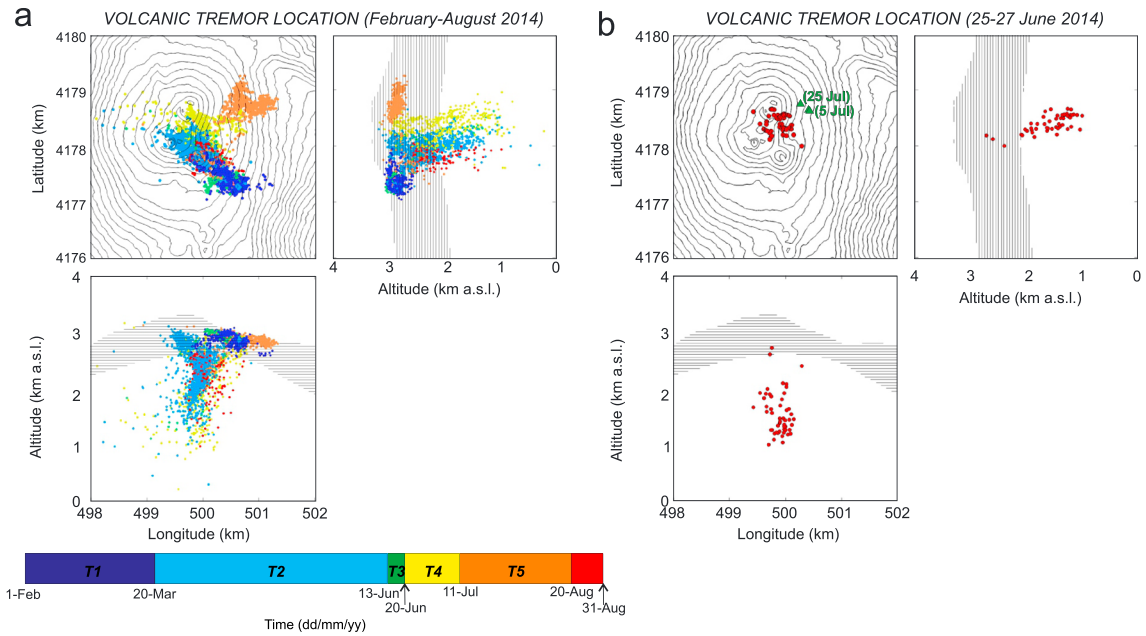

Figure 4. (a) Map and sections of Mount Etna with location of the volcanic tremor centroids during February–August 2014. The color of the dots relates to different times (see Figure 2d). (b) Map and sections of Mount Etna with location of the volcanic tremor centroids during 25–27 June 2014. The green triangles in the map indicate the vents opened on 5 and 25 July.

with similar intensity [e.g. *Battaglia et al*., 2005a, 2005b; *Cannata et al*., 2013]. For this reason, in this work the volcanic tremor locations are referred to as tremor centroids.

The relationship between tremor and volcanic activity is shown in Figure 2. The amplitude of volcanic tremor increased during eruptive periods (Figures 2a and 2c), and the centroids migrated toward the active vents (Figures 2a, 2d, and 4a). Accordingly, during February–March (T1), mid-June (T3), and mid-August (final part of T5), explosive and effusive activities at NSEC correlate with fairly high values of RMS and shallow volcanic tremor sources located in the NSEC area. Similarly, during the activity at the eruptive fissure at the base of NEC (early July to early August; initial part of T5), the source centroid of volcanic tremor migrated toward the eruptive vents, becoming shallower, and high RMS values were also observed.

One of the very few intervals, characterized by deep volcanic tremor and almost complete lack of shallow tremor, was 25–27 June (during T4), when the centroids were mainly clustered east of VOR and NEC at depth 1–2 km asl ± 0.7 km (dashed black rectangle in Figures 2c, 2d, and 4b).

4. Petrological Characteristics of the Erupted Products

4.1. Sampling and Analytical Methods

Ten air-quenched lava samples were taken at the fissure at the base of NEC on 28 July 2014 (midpart of T5) and at NSEC on 14 August 2014 (final part of T5) from the upper part of active lava flows (Figure 1b). Twenty-two plagioclase and 16 olivine crystals, representative of crystal textural variability, were selected for petrological analyses. We measured An% and FeO wt % composition along core-to-rim profiles of the plagioclase crystals, for each textural type and Fo% variations along core-to-rim transects, for olivine crystals. Spacing between individual analysis spots in all crystals ranges between 5 and 10 μm depending on crystal sizes. High-resolution backscattered electron images (BSE, 1024 · 864 pixels) and microanalytical data on plagioclase, olivine, and the other mineral phases were obtained on polished thin sections at the Dipartimento di Scienze Biologiche, Geologiche e Ambientali, University of Catania (Italy) using a Tescan Vega-LMU scanning electron microscope equipped with an EDAX Neptune XM 4–60 microanalyzer operating by energy dispersive system characterized by an ultrathin Be window coupled with an EDAX WDS LEXS (wavelength dispersive low-energy X-ray spectrometer) calibrated for light elements. Operating conditions were set at 20 kV accelerating voltage to obtain high-contrast BSE images and the analysis of major element abundances in mineral phases. Repeated analyses on internationally certified An-rich plagioclase, Fo-rich olivine, and glass inner standards during the analytical runs ensure precision for all the collected elements in the order of 3–5%.

4.2. Petrographic Features of the Volcanic Rocks

Bulk rock compositions of lavas emitted during the July–August 2014 activity are K-trachybasalts, similar in composition to other post-2011 products erupted at Mount Etna [*Behncke et al*., 2014; *Viccaro et al*., 2014, 2015]. Clasts are highly vesicular (45 vol % bubbles), porphyritic with seriate texture and phenocryst content varying between 15% and 20% in volume. Clasts textures are vitrophyric to locally hyalopilitic. In the crystallized portions, microlites (size <100 μm) are generally constituted by acicular plagioclase, augitic clinopyroxene, subordinate olivine, and oxides. Phases >100 μm (microphenocrysts and phenocrysts) are plagioclase (45–50 vol %), clinopyroxene (~30 vol %), olivine (~15–20 vol %), and oxides (<5 vol %). Textural characteristics of plagioclase and olivine crystals are described in detail in the next sections. Clinopyroxene is euhedral to subhedral with grain size generally ranging between ~100 μm (microphenocrysts) and ~2 mm. Larger crystals can be found as single individuals or in aggregates with other mineral phases. Clinopyroxene compositions were determined by SEM-EDS/WDS analyses; compositionally, most clinopyroxenes fall within the augite field with less common clinopyroxenes falling within the diopside-salite field. These features are on the whole similar to those of other clinopyroxenes found in recent lavas from Mount Etna [*Viccaro et al*., 2015]. Some augitic clinopyroxenes show embayed disequilibrium textures at the rim. Oxides are generally subhedral to anhedral small in size (50–200 μm) and classified as titaniferous magnetite. They are frequently enclosed in olivine and clinopyroxene minerals, testifying to their early nucleation and growth. Textural relationships suggest a sequence of crystallization of titaniferous magnetite followed by olivine, augitic clinopyroxene, and finally plagioclase.

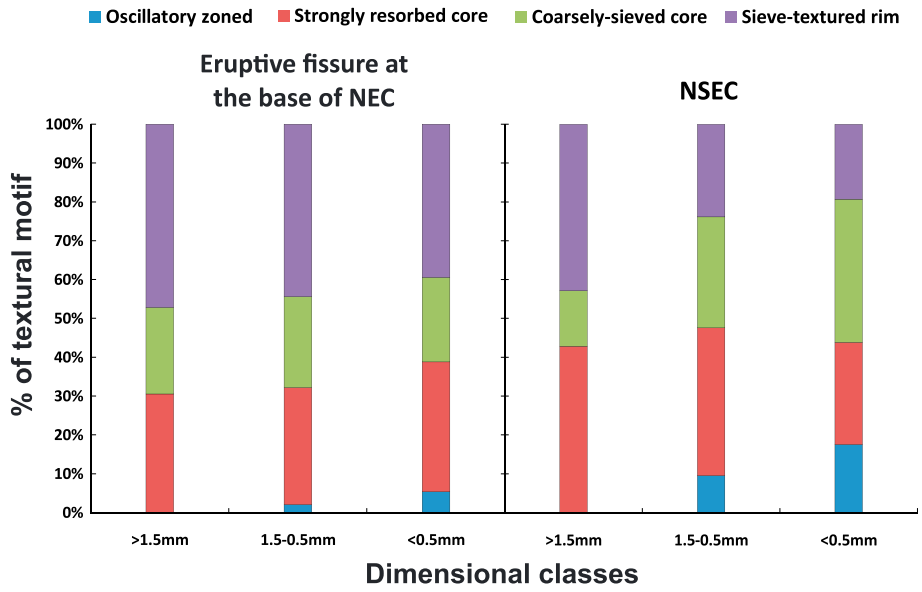

Figure 5. Histograms of the textural motif percentages (oscillatory zoning, strongly resorbed core, coarsely sieved core and sieved rim) for plagioclase crystals found in volcanic products of the eruptive fissure at the base of NEC and NSEC. Percentages of textural motifs have been considered in relation to the three main dimensional classes based on the length of the apparent *c* axis (i.e., >1.5 mm, 1.5 mm–0.5 mm, <0.5 mm).

4.3. Textural and Compositional Features of Plagioclase Crystals

Plagioclase crystal compositions from lavas erupted at the base of NEC and NSEC during the period July–August 2014 (T5) range between An_{91} and An_{40} (Table S1). Three size classes have been identified on the basis of the length of the apparent *c* axis: large $c > 1.5$ mm, intermediate *c* 0.5–1.5 mm, and small $c < 0.5$ mm. For each dimensional class, textural analysis highlighted four main textures: (1) oscillatory zoning, (2) strongly resorbed cores, (3) coarsely sieved core, and (4) sieve textures at the rim. Frequency of the textural types in relation to the dimensional classes is reported in Figure 5.

The wholly oscillatory zoning pattern is the least abundant pattern and not present in the largest crystals (Figure 5). This texture is characterized by generally high An contents ($An_{80\text{-}90}$, except one crystal of NEC with An_{53}; see also Table S1). Zoning patterns consist of limited fluctuations of the An content ($<\Delta An_5$) with high frequency of the oscillations (LAHF, low amplitude high frequency in *Viccaro et al.* [2010]), although sporadic crystals with slightly more pronounced An oscillations at lower frequency were observed (high amplitude low frequency in *Viccaro et al.* [2010]; Figures 6 and 7). FeO ranges between 0.7 and 1.0 wt % with trends generally concordant with An. It is worth noting that the behavior of An% and FeO wt % toward the crystal rims can be different. Plagioclase crystals in lavas at the base of NEC exhibit a sudden An drop in the last 10–35 μm down to $An_{40\text{-}50}$ (Figures 6c and 6d). On the contrary, crystals pertaining to NSEC products have a gradual decrease of the An content in the 50–70 μm outer rims, characterized by flat zones at An_{70} and An_{60} (Figure 7). FeO displays an increase from 0.8 up to 1.0 wt %.

The two most abundant core textures in all classes are strong resorption or coarsely sieve textures (Figure 5). In both cases, the texture is characterized by randomly distributed micrometric glass inclusions: strongly resorbed cores appear as dusty cores, whereas coarsely sieve textures produce less pervasive resorption at the cores. Crystals with these two textural types have average An values around 80%, which are fairly constant throughout the disequilibrium zone; iron generally varies within a narrow range between 0.7 and 0.8 wt %, with some crystals showing peaks at 0.6–1.0 wt % (Figures 6 and 7 and Table S1).

Some crystals display sieved textures at the rim (Figures 6a, 6b, 7a, and 7b). This texture comprises around 40% to 45% of crystals in lavas from the base of NEC; larger NSEC crystals display 40% of sieve texture at their rims, whereas intermediate and small size plagioclases have lower proportions of this texture (~20%; Figure 5). Anorthite is fairly constant or decreases slightly inside the sieve-textured zones, whereas FeO wt % has generally increasing trends or is otherwise constant. Some crystals found in lavas at the base of NEC have lower An

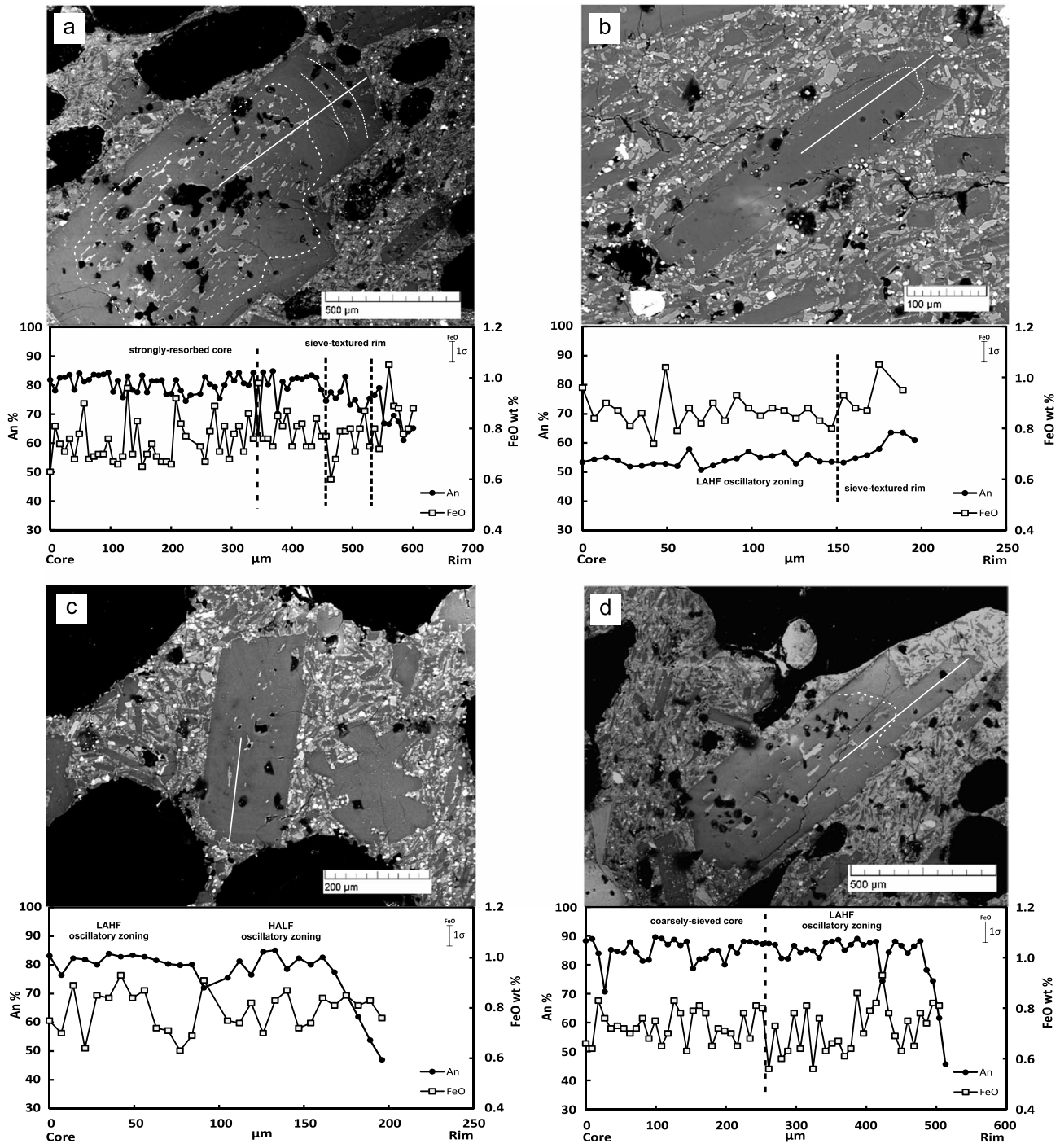

Figure 6. High-contrast BSE images of plagioclase crystals with various textures and their associated core-to-rim profile for An% (black circles) and FeO wt % (white squares) found in the volcanic products emitted by the eruptive fissure at the base of NEC.

contents at their cores (~An_{53}) and exhibit concordant increase of An% and FeO wt % at the sieved zone at the rim (Figure 6b).

4.4. Compositional Zoning of Olivine Crystals

Olivine crystals are generally <1.5 mm in size, with rare larger crystals (~3 mm) observed chiefly in the NSEC lavas. Olivine crystals can also exhibit resorption textures such as embayments. The composition of olivine

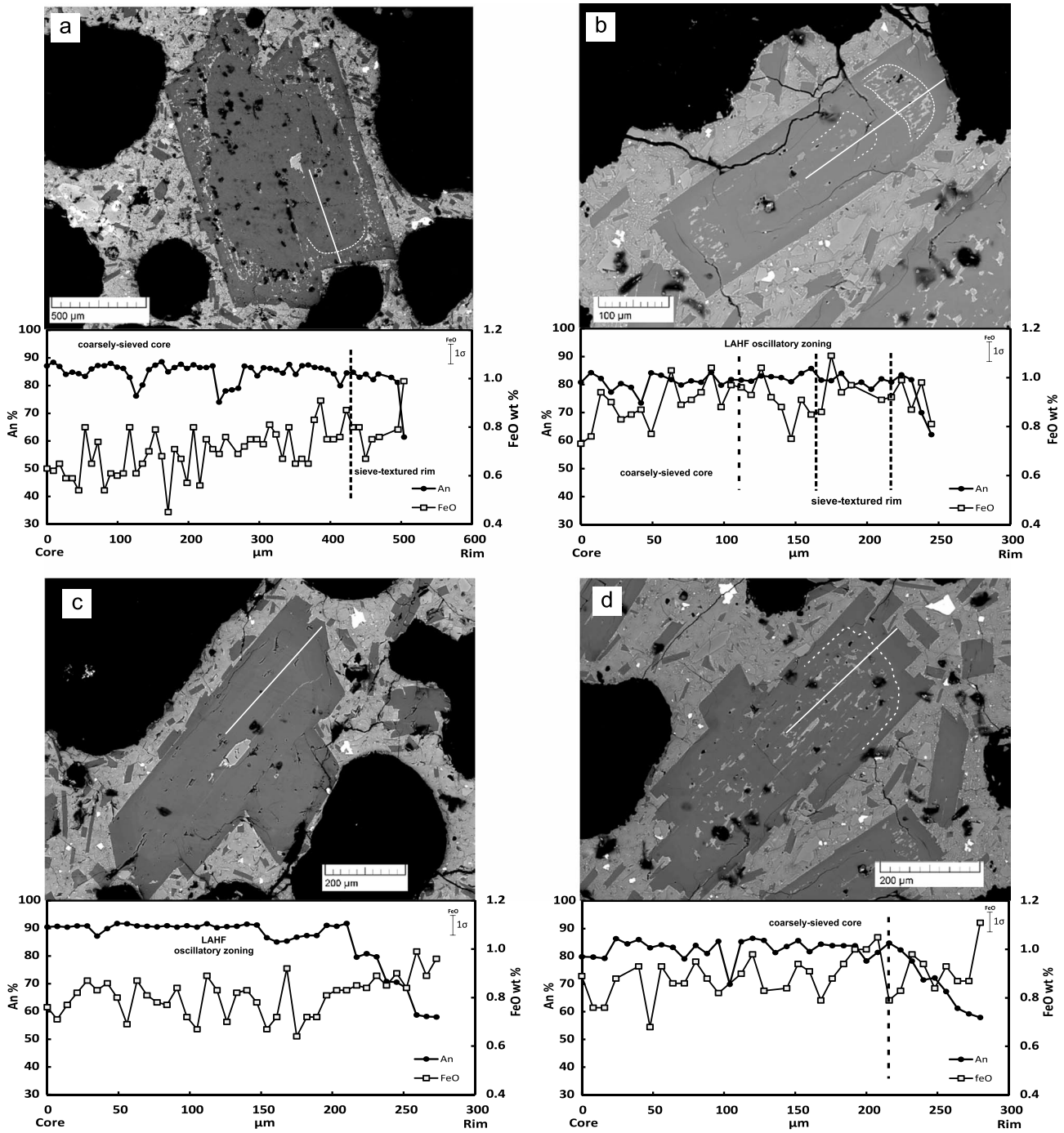

Figure 7. High-contrast BSE images of plagioclase crystals with various textures and their associated core-to-rim profile for An% (black circles) and FeO wt % (white squares) found in the volcanic products of NSEC.

crystals in the lavas of the July–August 2014 emitted both at the base of NEC and NSEC ranges between Fo_{86} and Fo_{71} (Figures 8 and 9 and Table S2). The occurrence of Fo_{86} olivine is, however, restricted to only one crystal found in lavas from the base of NEC. The most abundant olivine population has $Fo_{82\text{-}84}$ at the core and normal zoning (i.e., decreasing Fo% toward the rim). Some olivine crystals from both eruptive systems display lower forsterite contents at their cores ($Fo_{75\text{-}78}$; Figures 8h and 9h). Olivine rims have larger variability than cores: in lavas at the base of NEC, olivine rims range between Fo_{79} and Fo_{71}, whereas olivine crystals of NSEC lavas have values at $Fo_{76\text{-}78}$, with occasional crystals characterized by slightly lower values at Fo_{74}

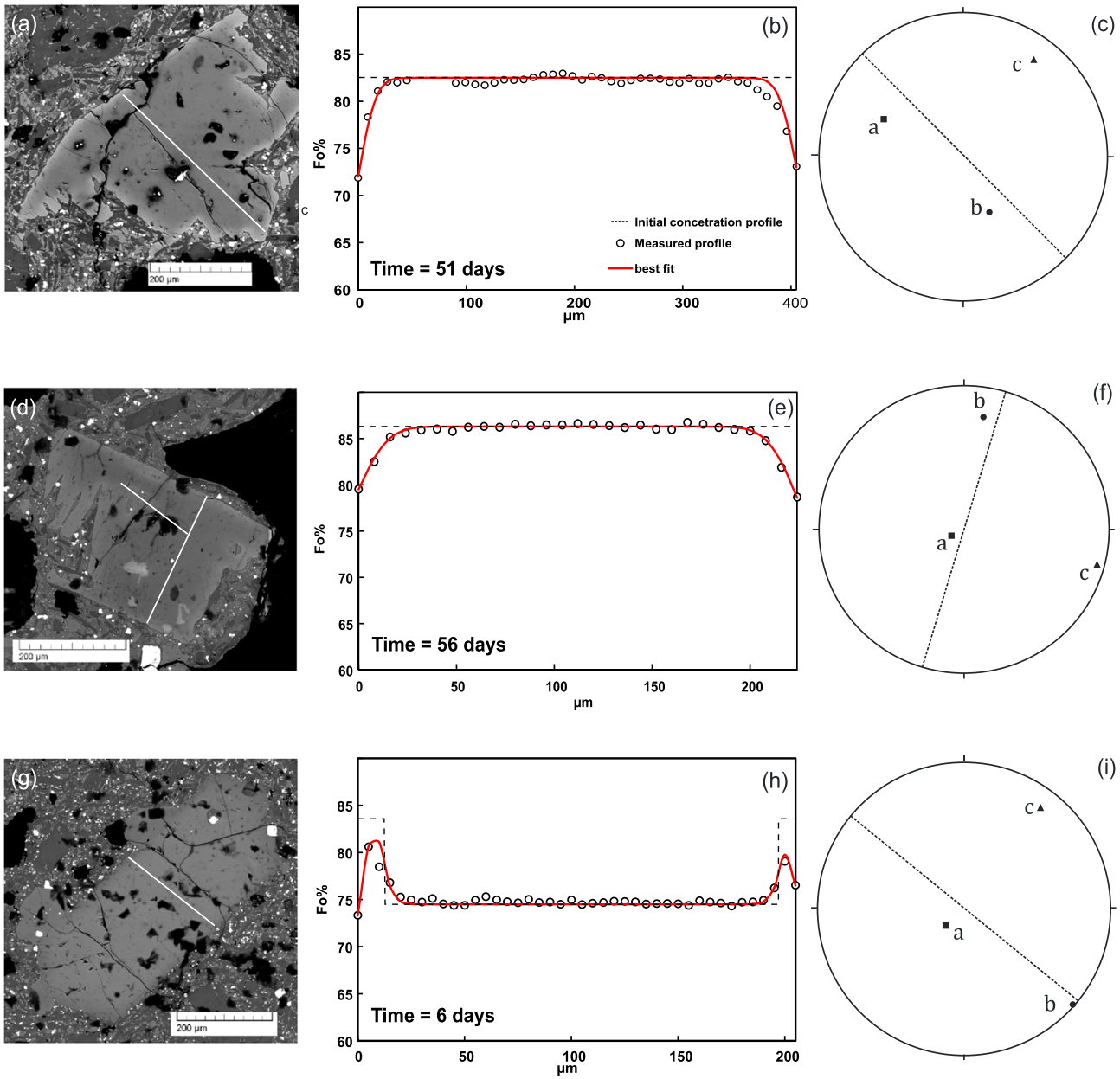

Figure 8. BSE images (a, d, g), rim-to-rim profiles for the measured Fo% (white circles), and Fe-Mg diffusion modeling (red lines) for representative olivine crystals found in lavas emitted by the eruptive fissure at the base of NEC (b, e, h). Black dashed lines indicate the initial concentration profile prior to the diffusion, whereas red lines reveal the best fit diffusion model (related to a specific timescale) for the observed zoning profile. The stereographic plot (c, f, i) indicates the angular relations between the *a*, *b*, and *c* crystallographic axes in olivine and the directions of the measured rim-to-rim traverse (dashed lines in circles).

(Figures 8 and 9). In rare instances, reverse zoning (i.e., increasing Fo toward the rim) occurs in products from both the eruptive systems. Reverse zoning is more evident in olivines from the base of NEC, which has Fo_{75} cores and increasing up to $Fo_{80\text{-}81}$ at the rim (Figure 8h).

5. Discussion

5.1. Discussion of Geophysical Data

Analysis of volcanic tremor during February–August 2014 at Mount Etna shows a correlation over time and space with volcanic activity, a result seen at other volcanoes worldwide [e.g., *McNutt*, 1994; *Battaglia et al.*, 2005a, 2005b; *McNutt and Nishimura*, 2008]. First, the location of volcanic tremor centroids changes with

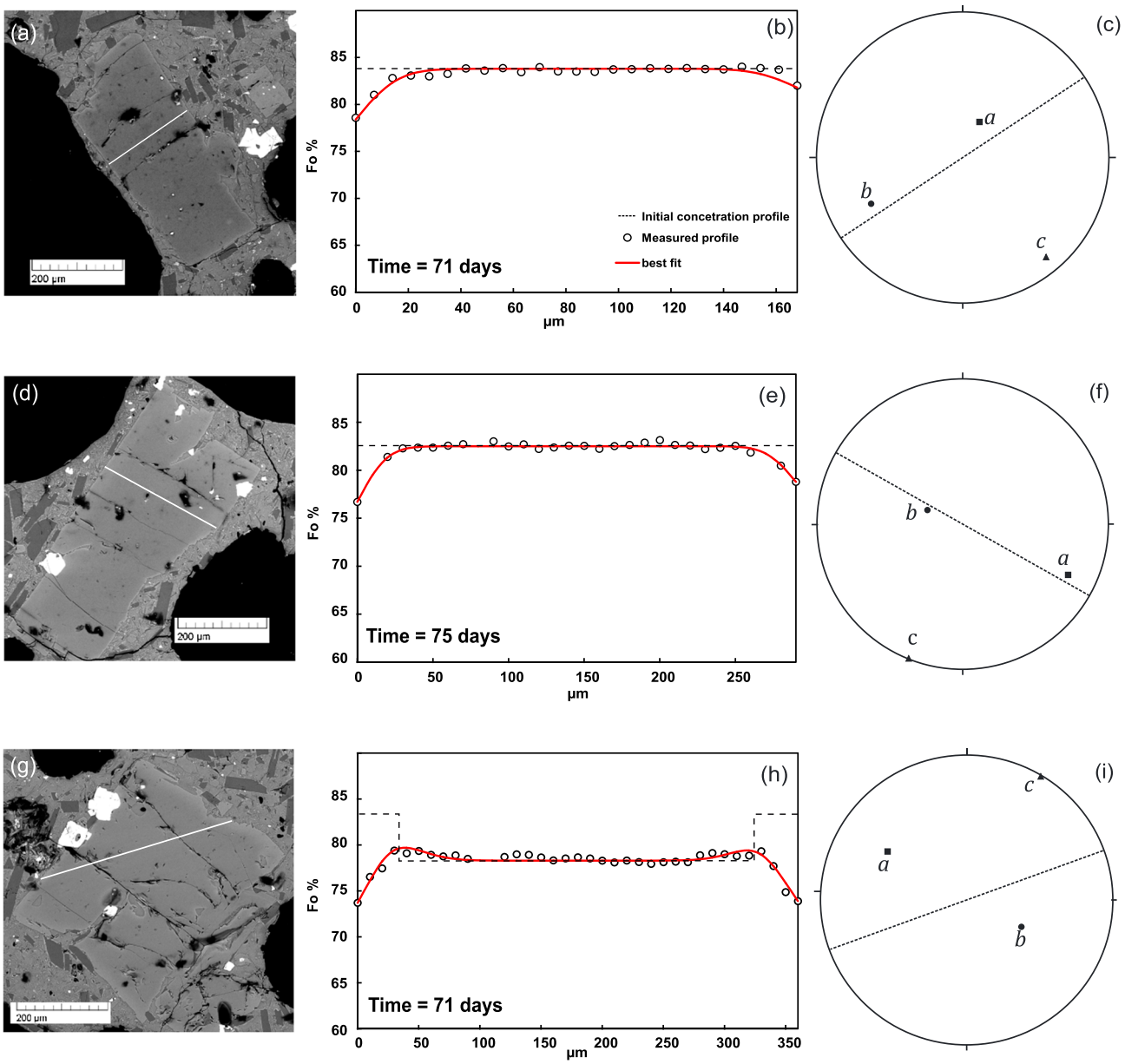

Figure 9. BSE images (a, d, g), rim-to-rim profiles for the measured Fo% (white circles), and Fe-Mg diffusion modeling (red lines) for representative olivine crystals found in lavas emitted by the eruptive fissure at the base of NSEC (b, e, h). Black dashed lines indicate the initial concentration profile prior to the diffusion, whereas red lines reveal the best fit diffusion model (related to a specific timescale) for the observed zoning profile. The stereographic plot (c, f, i) indicates the angular relations between the *a*, *b*, and *c* crystallographic axes in olivine and the directions of the measured rim-to-rim traverse (dashed lines in circles).

active vent locations (Figures 2d and 4a). The most evident migration was observed on 10 August (during T5), when the centroids moved southward from vents located at the base of the NEC toward NSEC, reflecting the spatial shift of the explosive activity (Figures 2a, 2d, and 4a). Second, the tremor amplitude reflects variations in explosive intensity: the more intense the explosive activity, the higher the amplitude. The highest values of amplitude were observed during the NSEC eruptive episode in mid-June (T3) and during the 25 July to 10 August (during T5) period at the base of NEC, which were both characterized by strong Strombolian activity (Figures 2a and 2c).

Volcanic tremor locations at Mount Etna have also been used to reconstruct the geometry of the plumbing system [e.g., *Patanè et al.*, 2008, 2013]. During part of the time interval investigated in this work (such as T1, T3, and T5), the tremor centroids were shallow and roughly located at the eruptive vents, which can be

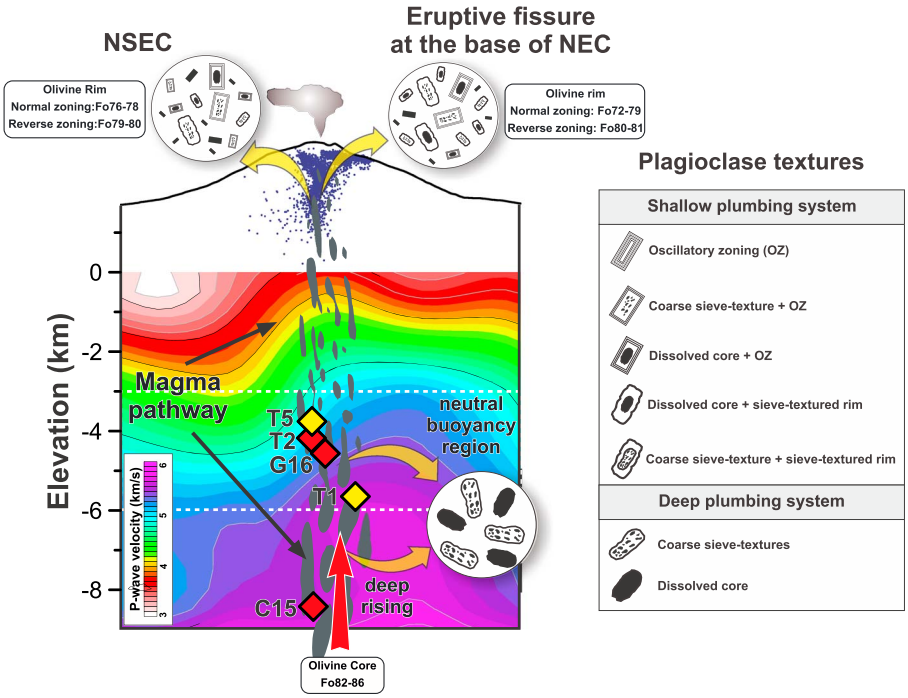

Figure 10. Simplified sketch model of the Mount Etna plumbing system (E-W cross section). Sources modeled in this study (T1, T2, and T5) as well as those obtained for previous (C15 [*Cannata et al*., 2015]) and successive (G16 [*Gambino et al*., 2016]) time intervals are indicated with diamonds: inflating sources are colored in red while the deflating ones are reported in yellow. The location of the volcanic tremor centroids, inferred for the February–August 2014 time interval, is also reported as blue dots. *P* wave velocity tomography is reported as background [*Chiarabba et al*., 2000]. In the sketch there is also information on the textures of plagioclase crystals and the olivine compositions in the deep portion of the Mount Etna plumbing system, which are fairly comparable in products from the two eruptive systems. Conversely, textural and compositional differences observed at the plagioclase and olivine rims from the eruptive fissure at the base of NEC and NSEC indicate distinct crystallization conditions at shallower levels.

considered the shallowest parts of the plumbing system. During noneruptive periods (such as T2 and T4), thanks to the lack of shallow prevailing tremor sources, we were able to locate deeper sources and then highlight the deeper portion of the plumbing system (Figures 2d and 4a). One of the intervals characterized by both deep volcanic tremor sources and almost complete lack of shallow sources was 25–27 June (during T4), when the centroids migrated slightly east of VOR and NEC areas (dashed black rectangle in Figures 2c, 2d, and 4b), at 1–2 km asl. These centroids are likely to highlight a portion of plumbing system, which successively fed the activity at the base of NEC, as suggested by both the proximity of this tremor source with the vent (Figure 4b) and the time relationship (the activity at the base of NEC started less than 10 days after this migration; Figures 2a and 2d).

Constraints on the magma movement in the deeper parts of the plumbing system are provided by GPS-based ground deformation data (Figure 2b). In response to lava effusion from vents located on the eastern flank of NSEC during the first 3 months of 2014, GPS data showed deflation (T1; Figures 3a and 3b), followed by a new pressurizing of the plumbing system from 20 March to 14 June (T2; Figures 3c and 3d). For T1, the modeled source is located beneath the summit area at a depth of ~5.6 km bsl, while T2 has been modeled as the pressurization of a near vertical elongated spheroidal source centered at ~4.2 km bsl beneath the upper western flank of the volcano, ~1.4 km shallower than the deflation source for T1 (Figure 10). The inflation abruptly ended on 14 June at the start of a short-lived eruption at NSEC (T3; Figures 2a and 2b) with corresponding deflation in the summit area and an abrupt south-eastward migration of the tremor source toward NSEC area (similar location to the one observed during T1 activity; Figures 2d and 4a). Indeed, some small amplitude lengthening/shortening variations (related to small inflation/deflation episodes) can be detected from 14 June from the EPLU-EINT baseline time series. These episodes are only visible at the GPS stations close to the summit area (with a low signal/noise ratio), and we suppose that they might reflect magma

movements within shallow sources located slightly east of VOR and NEC area at 1–2 km asl, as highlighted by the volcanic tremor centroids during 25–27 June. After a slight inflationary period (T4), a clear deflation of the volcano edifice occurred during 11 July to 20 August (T5). This deflation is modeled as a prolate spheroid centered at ~3.7 km (bsl) beneath the summit area and dipping slightly toward NE (Figures 3e and 3f and Table 1).

Within the estimated uncertainties, the positions of sources modeled for T2 and T5 spatially overlap (Figure 10) and, therefore, these sources can reasonably be considered as a unique magmatic reservoir. Such a magmatic reservoir pressurized since late March 2014 (T2) and fed the volcanic activity during June–August at NSEC and at the eruptive fissure at the base of NEC. Successively, it depressurized (T5) due to eruptive activity. The small deflation/inflation episodes (T3 and T4), occurring from mid-June, might have affected the shallower plumbing system. In particular, during T4, especially from 25 to 27 June, the shallower plumbing system was delineated by volcanic tremor centroids located east of VOR and NEC areas at 1–2 km asl (Figures 2d and 4b). The small deflation/inflation episodes (T3 and T4) suggest that, during volcanic activity, the shallower reservoir experienced a drop in pressure which promoted refilling of the reservoir with fresh magma arising from the deep source located ~4 km bsl. This aspect is confirmed by petrological data discussed in the next section.

Finally, taking into account the sources inferred from the inversion of geodetic data in this study and those obtained for previous (2 May 2013 to 25 October 2013 [*Cannata et al*., 2015]) and successive [21 August 2014 to 25 December 2014; *Gambino et al*., 2016] time intervals, a progressive rising of their depths can be recognized (Figure 10). This fact suggests that volcanic activity since late 2013 was fed by a batch of fresh magma which, arising from a depth $>$ 8 km, accumulated in the magmatic reservoir located at a depth of ~4 km bsl (Figure 10), usually considered as the region of neutral buoyancy at Mount Etna and other basaltic volcanoes [*Ryan*, 1987; *Corsaro and Pompilio*, 2004].

5.2. Discussion of Petrological Data

5.2.1. Ascent and Storage Dynamics From Features of Plagioclase Crystals

Over 50% of plagioclase phenocryst cores found in the eruptive products from the base of NEC and NSEC show strongly resorbed or coarse sieve textures that indicate disequilibrium (Figures 5–7). As shown by several studies, plagioclase crystallization is enhanced as the system becomes saturated with sudden loss of water, whereas plagioclase stability is reduced under decreasing pressure at water-undersaturated conditions [e.g., *Nelson and Montana*, 1992; *Blundy and Cashman*, 2001, 2005, and references therein]. This means that the presence of H_2O dissolved in the melt assists plagioclase resorption resulting in development of sieve textures. *Nelson and Montana* [1992] demonstrated the relationships between the extent of resorption and the rate of decompression. Their experimental results suggest that plagioclase resorption depends closely on the magnitude of decompression: the higher ΔP, the higher the percentage of crystal resorption (evaluated as density of resorption channels in the crystal). If applied to the variety of core textures observed in Etnean plagioclases, variable rates of decompression experienced by magmas in the deep portions of the plumbing system could explain the occurrence of coarsely and strongly sieved cores [cf. *Viccaro et al*., 2010, 2014; *Nicotra and Viccaro*, 2012a, 2012b]. The comparable abundance of these textures in lavas erupted at the base of NEC and NSEC is an indication that the styles of magma ascent where plagioclase cores crystallize are rather similar for both systems. This suggests that, below a certain depth, magmas of the two systems experienced very similar crystallization histories. As shown by the aforementioned ground deformation data, the top of the deep magma source, common to both NEC and NSEC systems, could be located beneath the summit area at ~4 km bsl (Figure 10).

Occurrence of oscillatory zoning in plagioclase is associated to rates of reaction during crystallization [*Pearce and Kolisnik*, 1990; *Ginibre et al*., 2002]. Crystals of the July–August 2014 activity show, in particular, oscillation patterns characterized by low amplitude and high frequency (i.e., LAHF) of the An content throughout the core-to-rim profile (Figures 6 and 7). Several authors ascribed this behavior to crystallization kinetics at the crystal/melt interface in magmatic systems that are not affected by important changes of the chemical and/or physical conditions [cf. *Allegre et al*., 1981; *Ortoleva*, 1990; *Ginibre et al*., 2002; *Viccaro et al*., 2010]. Wholly oscillatory zoned crystals are absent in the larger plagioclase, but they occur in modest amounts in the intermediate and small dimensional classes (Figure 5). This suggests that growth in chemically and physically unperturbed conditions is, on the whole, rare.

Plagioclase rims not affected by disequilibrium show different compositional behavior in lavas from NEC and NSEC systems. In lavas from the base of NEC, normal zoning of An displays a sudden drop at the outer rim from An_{80-90} to as low as An_{40} (Figures 6c and 6d). In NSEC lavas the An content decreases more gradually toward the rim, with zones characterized by fairly constant An values (Figures 7c and 7d). In both these instances (Figures 7c and 7d), the An behavior is accompanied by an increase in iron, which strongly suggests changes in oxygen fugacity [*Longhi et al*., 1976; Phinney, 1992; *Bindeman et al*., 1998; *Wilke and Behrens*, 1999; *Sugawara*, 2001]. Experimental results have demonstrated that in plagioclase, iron is positively correlated with fO_2 such that the higher the oxygen fugacity, the higher the Fe content [*Bindeman et al*., 1998; *Wilke and Behrens*, 1999]. *Ruprecht and Wörner* [2007] also demonstrated that oxygen fugacity increases because of water exsolution; therefore, H_2O degassing is able to produce the observed discordant trends of An and iron at the plagioclase rims. The degassing styles of NEC and NSEC are not similar: NEC undergoes continuous degassing, whereas NSEC shows intermittent degassing probably due to conduit obstructions [*La Spina et al*., 2010]. Different degassing styles in NEC and NSEC conduits could therefore be responsible for the variable trends of normal zoning observed in the two suites of plagioclases at their rims. This could imply in turn that magmas underwent distinct chemical-physical conditions during their late crystallization history in the two conduits.

The percent of plagioclase crystals with sieve texture of rims is different in the two systems. In lavas from the base of NEC sieve-textured rim accounts for ~40% of the crystals, but in NSEC lavas only 20% (Figure 5). The constant An content, coupled with increase of iron inside the sieve textures, has been interpreted by some authors as due to gas injections that do not modify the evolutionary degree of the residing magma but have effects on the oxygen fugacity [*Bindeman et al*., 1998; *Wilke and Behrens*, 1999; *Ruprecht and Wörner*, 2007; *Viccaro et al*., 2014]. However, it is worth noting that these compositional changes in plagioclase are negligible, which can be indication of a limited extent of this phenomenon. Some small crystals, exclusively of lavas at the base of NEC, display sieve textures with a concordant, moderate increase of An and iron, features largely attributed to recharge by more basic magma (Figure 6b) [e.g., *Tsuchiyama*, 1985]. These plagioclases may be part of a residual batch of magma within the conduit of NEC that experienced a minor recharging episode by more basic magma before the eruption. Lower abundances of plagioclases with sieve textures in NSEC are further evidence for distinct crystallization dynamics within the two systems, at least for the upper parts of their conduits. Accordingly, the volcanic tremor source, which was detected at the end of June and located slightly east of VOR and NEC area at 1–2 km asl, might represent the shallow part of the plumbing system feeding the activity at the base of the NEC. Hence, the link between the two conduits (NEC and NSEC) could speculatively be located in a part of the plumbing system constrained between 1–2 km asl and 4 km bsl, where the common magmatic source is likely to be placed.

5.2.2. Timescales of Magmatic Processes From Diffusion Modeling of Olivine Zoning

Temporal constraints of magmatic processes in the shallow part of NEC and NSEC conduits were achieved following the approach of *Costa et al*. [2008] and *Costa and Morgan* [2010], who modeled the diffusion-controlled reequilibration of the Fe-Mg zoning in olivine (Figures 8 and 9). Crystals were preliminarily selected to minimize uncertainties on time determination due to the strong diffusion anisotropy related to the section orientation with respect to the fast diffusion direction (*c* axis). Anisotropy-corrected diffusivity along the direction of the profile was obtained taking into account how the compositional traverses were oriented with respect to the olivine crystallographic *a*, *b*, and *c* axes (respectively, coinciding with the optical indicatrix axes *Z*, *X*, and *Y* measured by conoscopic observations under a polarizing optical microscope equipped with a Zeiss 4 axis universal stage). Olivines selected for the modeling are those crosscut along crystallographic planes forming angles lower than 45° with the *c* axis. Accordingly, with *Costa and Chakraborty* [2004], these selection criteria should improve the accuracy and precision on time calculations. The modeling was performed using Fick's second law diffusion equation with concentration-dependent diffusion coefficients ($D_{Fe\text{-}Mg}$). We assumed the measured concentration at the rim of the crystals as boundary conditions (see Table S3 in the supporting information). The expression for calculating Fe-Mg diffusion coefficients along [001] is from *Dohmen and Chakraborty* [2007]. Coefficients for all the olivine crystals were calculated at temperature (T) = 1130°C, pressure (P) = 2500 bars, and oxygen fugacity (fO_2) at $10^{-9,98}$ bar (QFM buffer). Such parameters have been chosen in accordance with the T, P, and fO_2 values of olivine crystallization derived through MELTS simulations and are consistent with the range of crystallization conditions defined for the recent Etnean K-trachybasaltic magmas [*Viccaro et al*., 2015]. The adopted pressure value, which corresponds to ~ 7 km below the summit craters for an average density lithostatic load of 2.8 g/cm^3, was taken into

account on the basis of the inferred depth of the inflation source (cf. Table 1). Uncertainties of the model are mainly related to T and fO_2 determinations. The error propagation procedure follows the method adopted by *Kahl et al*. [2015] and was performed for temperature uncertainties of 1130°C ± 10°C and fO_2 of $10^{-9.98}$ bars ± 0.25 log (data in Table S3).

Awareness of the magmatic process causing diffusion in olivines is important to fix the initial composition of the diffusion modeling itself. The chemical records preserved in olivine cores ($Fo_{82\text{-}86}$ and $Fo_{75\text{-}78}$ for both the eruptive systems) are evidence of two compositionally distinct magmatic environments where crystals grew without important chemical-physical perturbations during the early stages of crystallization, as suggested by the flat core profiles (Figures 8 and 9). Later, as reflected in the rims, they developed chemical gradients as a consequence of changed conditions. The decreased Fo content at these crystal rims can be attributed to decompression-induced crystallization (which stabilizes more fayalitic olivine rims) and/or an interaction with degassed magmas within the NEC and NSEC conduits during the intrusion. This led to new conditions of equilibrium at lower Fo contents. Through the Fe-Mg diffusion model we estimated the timescale of this intrusion at shallower depth in the conduits (Table S3). The initial conditions of the model have been set considering the Fo contents in the flat portions at the olivine cores, i.e., before the change to more fayalitic compositions. Timescale calculations of the olivine zoning give 51–56 days in products from the base of NEC and ~ 75 days in NSEC lavas (before the respective dates of emission at the base of NEC-28 July and NSEC-14 August). These results indicate that all the analyzed olivine crystals encountered changing conditions in a period between the end of May and beginning of June. The eruptive event on 14–16 June at NSEC (T3), preceded by the moderate phase of inflation beginning on March 2014 (T2, Figure 2b), suggests that these olivine crystals may be a residue of a magma batch that was not erupted during June. Sporadic olivine crystals characterized by slight reverse zoning (from Fo_{78} to Fo_{80}, Figure 9h) were also found in the NSEC lavas. This could reflect interaction with more basic magma, whose crystallizing olivine is more forsteritic than the resident one. Excluding the sporadic olivine crystal at Fo_{86} found in lavas from the base of NEC, we have assumed that the olivines in equilibrium with the inferred more basic magma are those at $Fo_{82\text{-}84}$, which are the most representative population found in the NSEC crystals. Initial conditions to model the timescale of magma mixing have therefore been chosen considering an average of these values (Fo_{83}). Timescales of magma mixing resulting from the diffusion modeling give 71 days, which are consistent with mafic recharge before the event of 14–16 June.

In rare cases, olivine crystals in lavas from the base of NEC display reverse zoning with an increase of the Fo content from $Fo_{74\text{-}75}$ of the cores up to Fo_{80} at the rims (Figure 8h). In this case, reverse zoning has been attributed to recharge by a magma-bearing olivine with ~Fo_{84}, as observed in the most forsteritic cores of products from the base of NEC (average $Fo_{82\text{-}86}$). Modeling of the chemical zoning in these crystals provides an indication that interaction occurred ~6 days before the eruption that took place on 28 July (during T5) from the NEC fracture system. This minor event of magma injection suggested by petrological data is coherent with constraints provided by seismic and geodetic data during the period T5 (Figure 2b). Indeed, in this eruptive period, which is characterized by a volcano-wide deflation, we observed at least two minor inflation episodes. The first, between 16 and 30 July (during T5), has been attributed to refilling of the shallow reservoir (this could speculatively be associated with the portion of plumbing system at 1–2 km asl, inferred by volcanic tremor centroids during 25–27 June, during T4) by magma ascending from the source located at 4 km bsl, as imaged by geodetic data. Our findings also agree with the development of volcanic phenomena, which showed since 25 July an increase of the intensity and opening of a new vent at 3090 m asl on the lower flank of NEC.

6. Concluding Remarks

The integrated analysis of geodetic, seismic, and petrological data applied to a complex volcanic system like Mount Etna proved a powerful tool to gain insights on the spatial and temporal history of magma transfer and recharge beneath the volcano (Figure 10). In this work, the eruptive activity of July–August 2014 at the base of NEC and NSEC (T5) has been chosen as a case study to test the validity of this methodological approach. Our main findings can be summarized as follows:

1. Geodetic data give indications of a feeding source located at ~4 km bsl, which is unique for magmas erupted at the NEC and NSEC systems.
2. Volcanic tremor source locations enabled identifying shallow parts of the plumbing system at 1–2 km asl, likely feeding the activity at the base of NEC.

3. Textural and compositional data obtained on plagioclase crystals highlighted that deep dynamics of transfer are rather similar for magmas erupted at NEC and NSEC systems, but they differ as regards the chemical-physical conditions encountered at shallow levels. Differences have been attributed to distinct degassing styles experienced by magmas.
4. Timescales obtained through Fe-Mg diffusion modeling of the olivine zoning are consistent with a recharging phase by more mafic magma during late May to early June (T2) registered in crystals of products erupted from the base of NEC and NSEC, which is evidence of a common deep history of NEC and NSEC systems. Olivine zoning, however, suggests that significant injections of mafic magmas did not occur in the days preceding the eruption, but that only minor recharges were syn-eruptive.

Acknowledgments
We are grateful to the Associate Editor Mike Poland, the reviewers Cynthia Gardner and Frank Trusdell, and other two anonymous reviewers for their useful suggestions that greatly improved the paper. We are indebted to the technicians of the INGV-Osservatorio Etneo for enabling the acquisition of seismic and GPS data. The original data used in this manuscript are available from these authors: A. Cannata for seismic data (andrea.cannata@unipg.it), M. Palano for GPS data (mimmo.palano@ingv.it), and M. Viccaro for petrological data (m.viccaro@unict.it). The petrological part of this study was supported by the FIR 2014 research grant to Marco Viccaro from the University of Catania (Italy), grant 2F119B, title of the project "Dynamics of evolution, ascent and emplacement of basic magmas: Case studies from eruptive manifestations of Eastern Sicily."

References

Acocella, V., and M. Neri (2003), What makes flank eruptions? The 2001 Etna eruption and its possible triggering mechanisms, *Bull. Volcanol.*, *65*(7), 461–476.

Allegre, C. J., A. Provost, and C. Jaupart (1981), Oscillatory zoning: A pathological case of crystal growth, *Nature*, *294*, 223–229.

Andronico, D., et al. (2005), A multi-disciplinary study of the 2002–03 Etna eruption: Insights into a complex plumbing system, *Bull. Volcanol.*, *67*, 314–330, doi:10.1007/s00445-004-0372-8.

Andronico, D., M. D. Lo Castro, M. Sciotto, and L. Spina (2013), The 2010 ash emissions at the summit craters of Mt Etna: Relationship with seismo-acoustic signals, *J. Geophys. Res. Solid Earth*, *118*, 51–70, doi:10.1029/2012JB009895.

Barnie, T. D., et al. (2015), A multidisciplinary study of the final episode of the Manda Hararo dyke sequence, Ethiopia, and implications for trends in volcanism during the rifting cycle, in *Magmatic Rifting and Active Volcanism*, edited by T. J. Wright et al., *Geol. Soc. London Spec. Publ.*, 420.

Battaglia, J., K. Aki, and T. Staudacher (2005a), Location of tremor sources and estimation of lava output using tremor source amplitude on the Piton de la Fournaise volcano: 2. Estimation of lava output, *J. Volcanol. Geotherm. Res.*, *147*, 291–308.

Battaglia, J., K. Aki, and V. Ferrazzini (2005b), Location of tremor sources and estimation of lava output using tremor source amplitude on the Piton de la Fournaise volcano: 1. Location of tremor sources, *J. Volcanol. Geotherm. Res.*, *147*, 268–290.

Behncke, B., S. Branca, R. A. Corsaro, E. De Beni, L. Miraglia, and C. Proietti (2014), The 2011–2012 summit activity of Mount Etna: Birth, growth and products of the new SE crater, *J. Volcanol. Geotherm. Res.*, *270*, 10–21, doi:10.1016/j.jvolgeores.2013.11.012.

Bindeman, I. N., A. M. Davis, and M. J. Drake (1998), Ion microprobe study of plagioclase–basalt partition experiments at natural concentration level of trace elements, *Geochim. Cosmochim. Acta*, *62*, 660–676.

Blundy, J. D., and K. V. Cashman (2001), Ascent-driven crystallization of dacite magmas at Mount St. Helens, 1980–1986, *Contrib. Mineral. Petrol.*, *140*, 631–650.

Blundy, J. D., and K. V. Cashman (2005), Rapid decompression-driven crystallization recorded by melt inclusions from Mount St. Helens volcano, *Geology*, *33*, 793–796.

Böhm, J., A. Niell, P. Tregoning, and H. Schuh (2006), Global Mapping Function (GMF): A new empirical mapping function based on data from numerical weather model data, *Geophys. Res. Lett.*, *33*, B02406, doi:10.1029/2005GL025546.

Bonanno, A., M. Palano, E. Privitera, S. Gresta, and G. Puglisi (2011), Magma intrusion mechanisms and redistribution of seismogenic stress at Mt. Etna volcano (1997–1998), *Terra Nova*, *23*, 339–348, doi:10.1111/j.1365-3121.2011.01019.x.

Burton, M. R., et al. (2005), Etna 2004–2005: An archetype for geodynamically-controlled effusive eruptions, *Geophys. Res. Lett.*, *32*, L09303, doi:10.1029/2005GL022527.

Cannata, A., A. Catania, S. Alparone, and S. Gresta (2008), Volcanic tremor at Mt. Etna: Inferences on magma dynamics during effusive and explosive activity, *J. Volcanol. Geotherm. Res.*, *178*, 19–31, doi:10.1016/j.jvolgeores.2007.11.027.

Cannata, A., G. Di Grazia, M. Aliotta, C. Cassisi, P. Montalto, and D. Patanè (2013), Monitoring seismo-volcanic and infrasonic signals at volcanoes: Mt. Etna case study, *Pure Appl. Geophys.*, doi:10.1007/s00024-012-0634-x.

Cannata, A., G. Spedalieri, B. Behncke, F. Cannavò, G. Di Grazia, S. Gambino, S. Gresta, S. Gurrieri, M. Liuzzo, and M. Palano (2015), Pressurization and depressurization phases inside the plumbing system of Mount Etna volcano: Evidence from a multiparametric approach, *J. Geophys. Res. Solid Earth*, *120*, 5965–5982, doi:10.1002/2015JB012227.

Chiarabba, C., A. Amato, E. Boschi, and F. Barberi (2000), Recent seismicity and tomographic modeling of the Mount Etna plumbing system, *J. Geophys. Res.*, *105*(B5), 10,923–10,938, doi:10.1029/1999JB900427.

Chouet, B. (1996), Long-period volcano seismicity: Its source and use in eruption forecasting, *Nature*, *380*, 309–316.

Chouet, B. A., and R. S. Matoza (2013), A multi-decadal view of seismic methods for detecting precursors of magma movement and eruption, *J. Volcanol. Geotherm. Res.*, *252*, 108–175, doi:10.1016/j.jvolgeores.2012.11.013.

Corsaro, R. A., and M. Pompilio (2004), Buoyancy-controlled eruptions of magmas at Mt Etna, *Terra Nova*, *16*, 16–22.

Costa, F., and S. Chakraborty (2004), Decadal time gaps between mafic intrusion and silicic eruption obtained from chemical zoning patterns in olivine, *Earth Planet. Sci. Lett.*, *227*, 517–530.

Costa, F., and D. J. Morgan (2010), Time constraints from chemical equilibration in magmatic crystals, in *Timescales of Magmatic Processes: From Core to Atmosphere*, edited by A. Dosseto et al., pp. 125–159, Wiley, West Sussex.

Costa, F., R. Dohmen, and S. Chakraborty (2008), Timescales of magmatic processes from modeling the zoning patterns of crystals, in *Minerals, Inclusions and Volcanic Processes*, *Rev. Mineral. Geochem.*, vol. 69, edited by K. D. Putirka and F. J. Tepley III, pp. 545–594, Mineral. Soc. Am., Chantilly, Va.

Davidson, J. P., F. Tepley III, Z. Palacz, and S. Meffan-Main (2001), Magma recharge, contamination and residence times revealed by in situ laser ablation isotopic analysis of feldspar in volcanic rocks, *Earth Planet. Sci. Lett.*, *184*, 427–442.

Davidson, J. P., D. J. Morgan, B. L. A. Charlier, R. Harlou, and J. M. Hora (2007), Microsampling and isotopic analysis of igneous rocks: Implications for the study of magmatic systems, *Annu. Rev. Earth Planet. Sci.*, *35*, 273–311.

De Beni, E., B. Behncke, S. Branca, I. Nicolosi, R. Carluccio, F. D'Ajello Caracciolo, and M. Chiappini (2015), The continuing story of Etna's New Southeast Crater (2012–2014): Evolution and volume calculations based on field surveys and aerophotogrammetry, *J. Volcanol. Geotherm. Res.*, *303*, 175–186.

Di Grazia, G., S. Falsaperla, and H. Langer (2006), Volcanic tremor location during the 2004 Mount Etna lava effusion, *Geophys. Res. Lett.*, *33*, L04304, doi:10.1029/2005GL025177.

Dohmen, R., and S. Chakraborty (2007), Fe-Mg diffusion in olivine II: Point defect chemistry, change of diffusion mechanisms and a model for calculation of diffusion coefficients in natural olivine, *Phys. Chem. Miner.*, *34*, 409–430.

Druitt, T., F. Costa, E. Deloule, M. Dungan, and B. Scaillet (2012), Decadal to monthly timescales of magma transfer and reservoir growth at a caldera volcano, *Nature*, *482*, 77–82.

Dzurisin, D. (2007), *Volcano Deformation: Geodetic Monitoring Techniques*, 441 pp., Springer Praxis, Berlin.

Efron, B. (1982), *The Jackknife, the Bootstrap and Other Resampling Plans*, vol. 38, pp. 1–92, Soc. for Ind. and Appl. Math., Philadelphia, Pa., doi:10.1137/1.9781611970319.

Gambino, S., A. Cannata, F. Cannavò, A. La Spina, M. Palano, M. Sciotto, L. Spampinato, and G. Barberi (2016), The unusual 28 December 2014 dike-fed paroxysm at Mount Etna: Timing and mechanism from a multidisciplinary perspective, *J. Geophys. Res. Solid Earth*, *121*, 2037–2053, doi:10.1002/2015JB012379.

Ginibre, C., A. Kronz, and G. Wörner (2002), High resolution quantitative imaging of plagioclase composition using accumulated backscattered electron images: New constraints on oscillatory zoning, *Contrib. Mineral. Petrol.*, *142*, 436–448.

González, P. J., and M. Palano (2014), Mt. Etna 2001 eruption: New insights into the magmatic feeding system and the mechanical response of the western flank from a detailed geodetic dataset, *J. Volcanol. Geotherm. Res.*, *274*, 108–121, doi:10.1016/j.jvolgeores.2014.02.001.

Greco, F., G. Currenti, M. Palano, A. Pepe, and S. Pepe (2016), Evidence of a shallow persistent magmatic reservoir from joint inversion of gravity and ground deformation data: The 25–26 October 2013 Etna lava fountaining event, *Geophys. Res. Lett.*, 3246–3253, doi:10.1002/2016GL068426.

Herring, T. A., R. W. King, and S. C. McClusky (2010), *Introduction to GAMIT/GLOBK, Release 10.4*, pp. 1–48 , MIT Press, Cambridge.

Kahl, M., S. Chakraborty, F. Costa, and M. Pompilio (2011), Dynamic plumbing system beneath volcanoes revealed by kinetic modeling, and the connection to monitoring data: An example from Mt. Etna, *Earth Planet. Sci. Lett.*, *308*, 11–22.

Kahl, M., S. Chakraborty, F. Costa, M. Pompilio, M. Liuzzo, and M. Viccaro (2013), Compositionally zoned crystals and real-time degassing data reveal changes in magma transfer dynamics during the 2006 summit eruptions of Mt. Etna, *Bull. Volcanol.*, *75*, 692, doi:10.1007/s00445-013-0692-7.

Kahl, M., S. Chakraborty, M. Pompilio, and F. Costa (2015), Constraints on the nature and evolution of the magma plumbing system of Mt. Etna volcano (1991–2008) from a combined thermodynamic and kinetic modelling of the compositional record of minerals, *J. Petrol.*, *56*, 2025–2068.

La Spina, A., M. Burton, and G. G. Salerno (2010), Unravelling the processes controlling gas emission from the central and northeast craters of Mt. Etna, *J. Volcanol. Geotherm. Res.*, *198*, 368–376.

Longhi, J., D. Walker, and J. F. Hays (1976), Fe and Mg in plagioclase, Proceedings of the Luna Science Conference 7th, 1, 1281–1300.

Martí, J., A. Castro, C. Rodríguez, F. Costa, S. Carrasquilla, R. Pedreira, and X. Bolos (2013), Correlation of magma evolution and geophysical monitoring during the 2011–2012 El Hierro (Canary Islands) submarine eruption, *J. Petrol.*, *54*, 1349–1373.

Martini, F., F. Tassi, O. Vaselli, R. Del Potro, M. Martinez, R. Van del Laat, and E. Fernandez (2010), Geophysical, geochemical and geodetical signals of reawakening at Turrialba volcano (Costa Rica) after almost 150 years of quiescence, *J. Volcanol. Geotherm. Res.*, *198*, 416–432.

McNutt, S. R. (1994), Volcanic tremor amplitude correlated with the volcano explosivity index and its potential use in determining ash hazards to aviation, *Acta Vulcanol.*, *5*, 193–196.

McNutt, S. R., and T. Nishimura (2008), Volcanic tremor during eruptions: Temporal characteristics, scaling and constraints on conduit size and processes, *J. Volcanol. Geotherm. Res.*, *178*, 10–18.

Morgan, D. J., and S. Blake (2006), Magmatic residence times of zoned phenocrysts: Introduction and application of the binary element diffusion modeling (BDM) technique, *Contrib. Mineral. Petrol.*, *151*, 58–70.

Morgan, D. J., S. Blake, N. W. Rogers, B. De Vivo, G. Rolandi, R. Macdonald, and C. J. Hawkesworth (2004), Time scales of crystal residence and magma chamber volume from modeling of diffusion profiles in phenocrysts: Vesuvius 1944, *Earth Planet. Sci. Lett.*, *222*, 933–946.

Nelson, S. T., and A. Montana (1992), Sieve-textured plagioclases in volcanic rocks produced by rapid decompression, *Am. Mineral.*, *77*, 1242–1249.

Nicotra, E., and M. Viccaro (2012a), Unusual magma storage conditions at Mt. Etna (Southern Italy) as evidenced by plagioclase megacryst-bearing lavas: Implications for the plumbing system geometry and summit caldera collapse, *Bull. Volcanol.*, *74*, 795–815.

Nicotra, E., and M. Viccaro (2012b), Transient uprise of gas and gas-rich magma batches fed the pulsating behavior of the 2006 eruptive episodes at Mt. Etna volcano, *J. Volcanol. Geotherm. Res.*, *227–228*, 102–118.

Ortoleva, P. J. (1990), Role of attachment kinetic feedback in the oscillatory zoning of crystals growth from melts, *Earth Sci. Rev.*, *29*, 3–8.

Palano, M., G. Puglisi, and S. Gresta (1998), Ground deformation patterns at Mt. Etna from 1993 to 2000 from joint use of InSAR and GPS techniques, *J. Volcanol. Geotherm. Res.*, *169*, 99–120, doi:10.1016/j.jvolgeores.2007.08.014.

Palano, M., M. Rossi, C. Cannavò, V. Bruno, M. Aloisi, D. Pellegrino, M. Pulvirenti, G. Siligato, and M. Mattia (2010), Etn@ref: A geodetic reference frame for Mt. Etna GPS networks, *Ann. Geophys.*, *53*(4), 48–79, doi:10.4401/af-4879.

Patanè, D., G. Di Grazia, A. Cannata, P. Montalto, and E. Boschi (2008), The shallow magma pathway geometry at Mt. Etna volcano, *Geochem. Geophys. Geosyst.*, *9*, Q12021, doi:10.1029/2008GC002131.

Patanè, D., et al. (2013), Insights into magma and fluid transfer at Mount Etna by a multiparametric approach: A model of the events leading to the 2011 eruptive cycle, *J. Geophys. Res. Solid Earth*, *118*, 3519–3539, doi:10.1002/jgrb.50248.

Pearce, T. H., and A. M. Kolisnik (1990), Observation of plagioclase zoning using interference imaging, *Earth Sci. Rev.*, *29*, 9–26.

Phinney, W. C. (1992), Partitioning coefficients for iron between plagioclase and basalt as a function of oxygen fugacity: Implications for Archean and lunar anorthosites, *Geochim. Cosmochim. Acta*, *56*, 1885–1895.

Ruprecht, P., and G. Wörner (2007), Variable regimes in magma system documented in plagioclase zoning patterns: El Misti stratovolcano and Andahua monogenetic cones, *J. Volcanol. Geotherm. Res.*, *165*, 142–162.

Ryan, M. P. (1987), Neutral buoyancy and the mechanical evolution of magmatic systems, in *Magmatic Processes: Physicochemical Principles*, *Spec. Publ.*, vol. 1, edited by B. O. Mysen, pp. 259–287, Geochem. Soc., Univ. Park, Pennsylvania.

Saastamoinen, J. (1972), Contribution to the theory of atmospheric refraction, *Bull. Geod.*, *46*(3), 279–298.

Spampinato, L., S. Calvari, C. Oppenheimer, and L. Lodato (2008), Shallow magma transport for the 2002–3 Mt. Etna eruption inferred from thermal infrared surveys, *J. Volcanol. Geotherm. Res.*, *177*, 301–312.

Spampinato, L., M. Sciotto, A. Cannata, F. Cannavò, A. La Spina, M. Palano, G. G. Salerno, E. Privitera, and T. Caltabiano (2015), Multiparametric study of the February–April 2013 paroxysmal phase of Mt. Etna New South-East Crater, *Geochem. Geophys. Geosyst.*, *16*, 1932–1949, doi:10.1002/2015GC005795.

Streck, M. J. (2008), Mineral textures and zoning as evidence for open system processes, in *Minerals, Inclusions and Volcanic Processes*, *Rev. Mineral. Geochem.*, vol. 69, edited by K. D. Putirka and F. J. Tepley III, pp. 595–622, Mineral. Soc. Am., Chantilly, Va.

Sugawara, T. (2001), Ferric iron partitioning between plagioclase and silicate liquid: Thermodynamics and petrological applications, *Contrib. Mineral. Petrol.*, *141*, 659–686.

Tiampo, K. F., J. B. Rundle, J. Fernandez, and J. O. Langbein (2000), Spherical and ellipsoidal volcanic sources at Long Valley caldera, California using a genetic algorithm inversion technique, *J. Volcanol. Geotherm. Res.*, *102*(3), 189–206.

Tsuchiyama, A. (1985), Dissolution kinetics of plagioclase in the melt of the system diopside-albite-anorthite, and the origin of dusty plagioclase in andesites, *Contrib. Mineral. Petrol.*, *89*, 1–16.

Viccaro, M., P. P. Giacomoni, C. Ferlito, and R. Cristofolini (2010), Dynamics of magma supply at Mt. Etna volcano (Southern Italy) as revealed by textural and compositional features of plagioclase phenocrysts, *Lithos*, *116*, 77–91.

Viccaro, M., I. Garozzo, A. Cannata, G. Di Grazia, and S. Gresta (2014), Gas burst vs. gas-rich magma recharge: A multidisciplinary study to reveal factors controlling duration of the recent paroxysmal eruptions at Mt. Etna, *J. Volcanol. Geotherm. Res.*, *278–279*, 1–13.

Viccaro, M., R. Calcagno, I. Garozzo, M. Giuffrida, and E. Nicotra (2015), Continuous magma recharge at Mt. Etna during the 2011–2013 controls the style of volcanic activity and compositions of erupted lavas, *Miner. Petrol.*, *109*, 67–83, doi:10.1007/s00710-014-0352-4.

Viccaro, M., D. Barca, W. A. Bohrson, C. D'Oriano, M. Giuffrida, E. Nicotra, and B. W. Pitcher (2016a), Crystal residence times from trace element zoning in plagioclase reveal changes in magma transfer dynamics at Mt. Etna during the last 400 years, *Lithos*, *248-251*, 309–323.

Viccaro, M., M. Giuffrida, E. Nicotra, and R. Cristofolini (2016b), Timescales of magma storage and migration recorded by olivine crystals in basalts of the March–April 2010 eruption at Eyjafjallajökull volcano, Iceland, *Am. Mineral.*, *101*, 222–230.

Wilke, M., and H. Behrens (1999), The dependence of the partitioning of iron and europium between plagioclase and hydrous tonalitic melt on oxygen fugacity, *Contrib. Mineral. Petrol.*, *137*, 102–114.

Williams, C. A., and G. Wadge (2000), An accurate and efficient method for including the effects of topography in three-dimensional elastic models of ground deformation with applications to radar interferometry, *J. Geophys. Res.*, *105*(B4), 8103–8120, doi:10.1029/1999JB900307.

Yang, X. M., P. M. Davis, and J. H. Dieterich (1988), Deformation from inflation of a dipping finite prolate spheroid in an elastic half-space as a model for volcanic stressing, *J. Geophys. Res.*, *93*(B5), 4249–4257, doi:10.1029/JB093iB05p04249.

Zellmer, G. F., S. Blake, D. Vance, C. Hawkesworth, and S. Turner (1999), Plagioclase residence times at two island arc volcanoes (Kameni island, Santorini, and Soufriere, St. Vincent) determined by Sr diffusion systematics, *Contrib. Mineral. Petrol.*, *136*, 345–357.

Zellmer, G. F., R. S. J. Sparks, C. J. Hawkesworth, and M. Wiedenbeck (2003), Magma emplacement and remobilization timescales beneath Montserrat: Insights from Sr and Ba zonation in plagioclase phenocrysts, *J. Petrol.*, *44*, 1413–1431.